Physics of Fluids

RESEARCH ARTICLE | DECEMBER 08 2023

Aerodynamic mechanism of a combined buffer hood for mitigating micro-pressure waves at the 400 km/h high-speed railway tunnel portal

Guo-Zhi Li (李国志) ; Xin Ye (叶昕) ; E Deng (邓锷) ; Wei-Chao Yang (杨伟超); Yi-Qing Ni (倪一清) ; Hong He (何洪) ; Wai-Kei Ao (区玮玑)

Check for updates

Physics of Fluids 35, 126106 (2023)
https://doi.org/10.1063/5.0177766

View Online
Export Citation

Articles You May Be Interested In

Influence of arch lattice-shell hood length on micro-pressure waves at portal of a high-speed maglev tunnel

Physics of Fluids (September 2024)

Mitigation mechanism of porous media hood for the sonic boom emitted from maglev tunnel portals

Physics of Fluids (October 2024)

Pressure amplification effect of initial compression waves in circumferential cracks of high-speed railway tunnel linings

Physics of Fluids (June 2023)

08 January 2025 07:45:32

AIP Publishing
Physics of Fluids
Special Topics Open for Submissions
Learn More

AIP Publishing

Aerodynamic mechanism of a combined buffer hood for mitigating micro-pressure waves at the 400 km/h high-speed railway tunnel portal

Cite as: Phys. Fluids **35**, 126106 (2023); doi: 10.1063/5.0177766
Submitted: 24 September 2023 · Accepted: 12 November 2023 ·
Published Online: 8 December 2023

View Online Export Citation CrossMark

Guo-Zhi Li (李国志),[1] Xin Ye (叶昕),[2,3] E Deng (邓锷),[2,3,a)] Wei-Chao Yang (杨伟超),[1,4] Yi-Qing Ni (倪一清),[1,3] Hong He (何洪),[1] and Wai-Kei Ao (区玮玑)[2,3]

AFFILIATIONS

[1]School of Civil Engineering, Central South University, Changsha, People's Republic of China
[2]National Rail Transit Electrification and Automation Engineering Technology Research Center (Hong Kong Branch), Hong Kong, People's Republic of China
[3]Department of Civil and Environmental Engineering, The Hong Kong Polytechnic University, Hong Kong, People's Republic of China
[4]National Engineering Research Center of High-speed Railway Construction Technology, Changsha, People's Republic of China

[a)]**Author to whom correspondence should be addressed:** early.deng@polyu.edu.hk

08 January 2025 07:45:32

ABSTRACT

As high-speed trains exceed 400 km/h, tunnel aerodynamics pose significant challenges. The hat oblique tunnel buffer hood with enlarged cross section and ventilation windows (HEW) is a promising solution to mitigate micro-pressure waves (MPWs). However, there is limited research on HEW ventilation window configurations. Thus, field measurements and numerical simulations were conducted using the slip grid technique and an improved delayed eddy simulation turbulence model, with validation against field data. The study investigated the effects of aperture rate and ventilation window arrangement, analyzing the initial compression wave, pressure gradient, MPW, and flow field in the tunnel buffer hood under various ventilation window setups. Findings emphasize that increasing the aperture rate or placing ventilation windows near the tunnel entrance reduces MPWs when a high-speed train enters the buffer hood. However, it intensifies MPWs when the train transitions from the buffer hood to the tunnel. Optimal MPW mitigation is achieved with approximately 15% aperture rate and a ventilation window distance from the slope end of 0.3–0.4 times the enlarged cross section length. Double ventilation windows outperform single or three windows in MPW reduction, with longitudinally arranged windows at the top facilitating more efficient high-pressure air escape compared to circumferential windows.

Published under an exclusive license by AIP Publishing. https://doi.org/10.1063/5.0177766

I. INTRODUCTION

With the rapid advancement of high-speed train (HST) construction technology, HST speeds are expected to surpass 400 km/h in the near future. The aerodynamic issues pertaining to tunnels are progressively gaining more prominence.[1,2] Among the challenges associated with tunnels, the generation of micro-pressure waves (MPWs) has become increasingly prominent.[3,4] In milder cases, the tunnel entrance produces a sonic boom that disrupts the daily lives of nearby residents, whereas, in more severe instances, it can even cause damage to nearby building structures.[5] To mitigate MPWs, the installation of a buffer hood at the tunnel entrance has been widely adopted. Traditional buffer hoods include the enlarged cross section hood,[6,7] linear horn hood,[8] gradient hood,[9,10] and hat oblique hood,[11] as shown in Fig. 1. However, these single hoods may face challenges in effectively controlling MPWs as HST speeds exceed 400 km/h. Simultaneously, some scholars have explored the combination of different single hoods. Among these combinations, HEW has garnered considerable attention from the engineering community. It combines the hat oblique buffer hood with an enlarged cross section and ventilation windows, presenting a promising new approach to hood design.

Previous studies[12] have validated the direct relationship between the peak of the micro-pressure wave (P_{MPW}) and the pressure gradient (PG) of the compression wave. The fundamental principle of the buffer hood is to extend the rise time of the compression wave, thus reducing the PG and effectively mitigating the P_{MPW}.[13] Scholars have demonstrated that the combined buffer hood exhibits a superior effect in

Published under an exclusive license by AIP Publishing

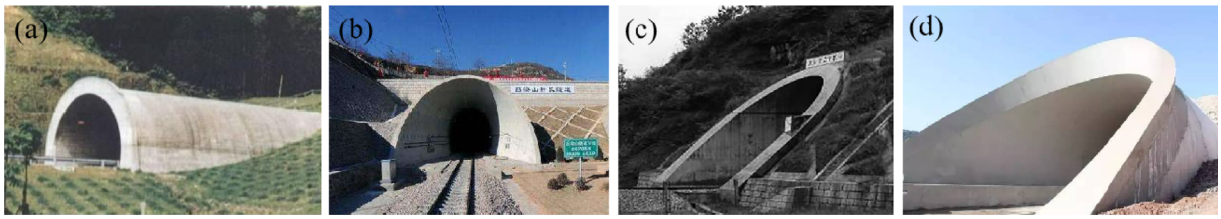

FIG. 1. Traditional buffer hoods: (a) enlarged cross section, (b) linear horn shape, (c) gradient, and (d) hat oblique.

reducing the PG in comparison with a single buffer hood. For instance, Xiang *et al.*[14] compared nine different types of buffer hoods, including a combination of a single enlarged cross section buffer hood with ventilation windows. They found that the size of the buffer hood and the ventilation window considerably influenced the peak of the initial compression wave (P_{ICW}). Other studies conducted by Saito[15] and Fukuda *et al.*[16] focused on the geometrical parameters of enlarged cross sections and the effect of ventilation windows on the PG, using model tests. Innovative approaches have also been explored. Kim *et al.*[17] designed a novel buffer hood with ventilation windows using biosimulation and modeling experiments. Their results demonstrated a remarkable reduction of 56.3% in the P_{ICW} and 78.7% in the P_{MPW} in comparison with traditional buffer hoods. Furthermore, the combination of ventilation windows with the hat oblique buffer hood has been extensively studied by various scholars. Zhang *et al.*[18,19] investigated the optimization of aperture rates for the aerodynamic buffering performance of a hat oblique buffer hood using numerical simulations and moving model experiments. Their findings revealed that an optimized ventilation window configuration led to a reduction of 50.22% in the peak of the pressure gradient (P_{PG}) and 51.22% in the P_{MPW} in comparison with scenarios without a buffer hood. Field measurements conducted by Liu *et al.*[20,21] compared the performance of the initial compression wave (ICW) and the MPW with and without ventilation windows in a hat oblique buffer hood. The results indicated a faster pressure wave decay rate in the tunnel and a remarkable reduction in the P_{MPW} when ventilation windows were present. These findings support the idea that a combination of a single buffer hood with ventilation windows enhances the buffering performance against MPWs. However, to mitigate effectively the MPWs generated by HST operating at speeds of 400 km/h or higher, further enhancements in buffer hood parameters are needed. The HEW, which incorporates elements such as an enlarged cross section, hat oblique buffer hood, and ventilation windows, presents a more suitable solution to address the challenges posed by increased train speeds.

The arrangement of ventilation windows plays a crucial role in mitigating MPW, and several scholars have extensively studied the rationality of their placement. Howe[22,23] elucidated the aerodynamic mechanism of the compression wave passing through ventilation windows and achieved an 80% reduction in PG by optimizing their position.[24] Xiang *et al.*[25] conducted a comprehensive investigation into the mitigation mechanism of MPW through ventilation windows using theoretical analysis and numerical simulations. They found that the aperture ratio of the ventilation window can be optimized by balancing the two P_{PGs} caused by the HST entering the tunnel and passing through the window. The aperture ratio is also influenced by the location and Mach number due to the superposition of compression waves. Heine *et al.*[26] visualized and analyzed the airflow characteristics of ventilation windows using particle image velocity measurement, providing insights into the airflow patterns and behavior associated with these windows. Miyachi *et al.*[27] combined moving model tests and theoretical analysis to optimize the mode and area of ventilation windows in a buffer hood. Their research demonstrated that the P_{PG} associated with the HST entering the buffer hood decreases linearly with an increase in the aperture rate, whereas the P_{PG} related to the train passing through the junction of the buffer hood and the tunnel increases linearly with the aperture rate. Okubo *et al.*[28] developed a fast and straightforward optimization method for ventilation windows in buffer hoods, adjusting the window height based on field measurements for an efficient optimization process. However, the actual control criteria for MPW may vary under different scenarios, considering factors such as train grouping, speed, terrain, and surrounding environment.[29] To promote the widespread use of the combined buffer hood in high-speed railway tunnels operating at 400 km/h, further in-depth studies are necessary to understand the specific MPW mitigation mechanisms of the HEW configuration.

This study uses the improved delayed detached eddy simulation (IDDES) turbulence model, in which the shear-stress transport (SST) k–ω model is applied in the near-wall region, to construct a three-dimensional computational fluid dynamics (CFD) dynamic grid simulation model of the tunnel–train–air system. The simulation method's reliability is verified through field measurements. The primary focus of the research is on the aperture rate and arrangement of ventilation windows within the buffer hood. It explores the effect of different ventilation window parameters on the ICW, PG, and MPW. Furthermore, the study investigates the buffering mechanism of the ventilation windows in the buffer hood, considering the combination of a hat oblique tunnel buffer hood with an enlarged cross section and ventilation windows, from the perspective of the flow field inside. The remaining chapters of this paper are as follows: Sec. II presents the Field Measurement, Sec. III discusses the Methodology, Sec. IV presents the Results and Discussion, and Sec. V provides the Conclusion.

II. FIELD MEASUREMENT

A. Measurement scheme

Field measurements were taken inside and outside a high-speed railway tunnel. Figure 2(a) provides an overview of the test site, where the tunnel has a length of 5931 m and a net cross-sectional area of 100 m^2. The train used for the measurements was an eight-car CRH380B HST. The speed limit in the tunnel is 350 km/h, and two tunnel buffer hoods were defined: hood A and hood B. Hood A consists of a 12 m-long enlarged cross section with two ventilation windows on the side, each measuring 4×4 m^2. By contrast, hood B is a

08 January 2025 07:45:32

Published under an exclusive license by AIP Publishing

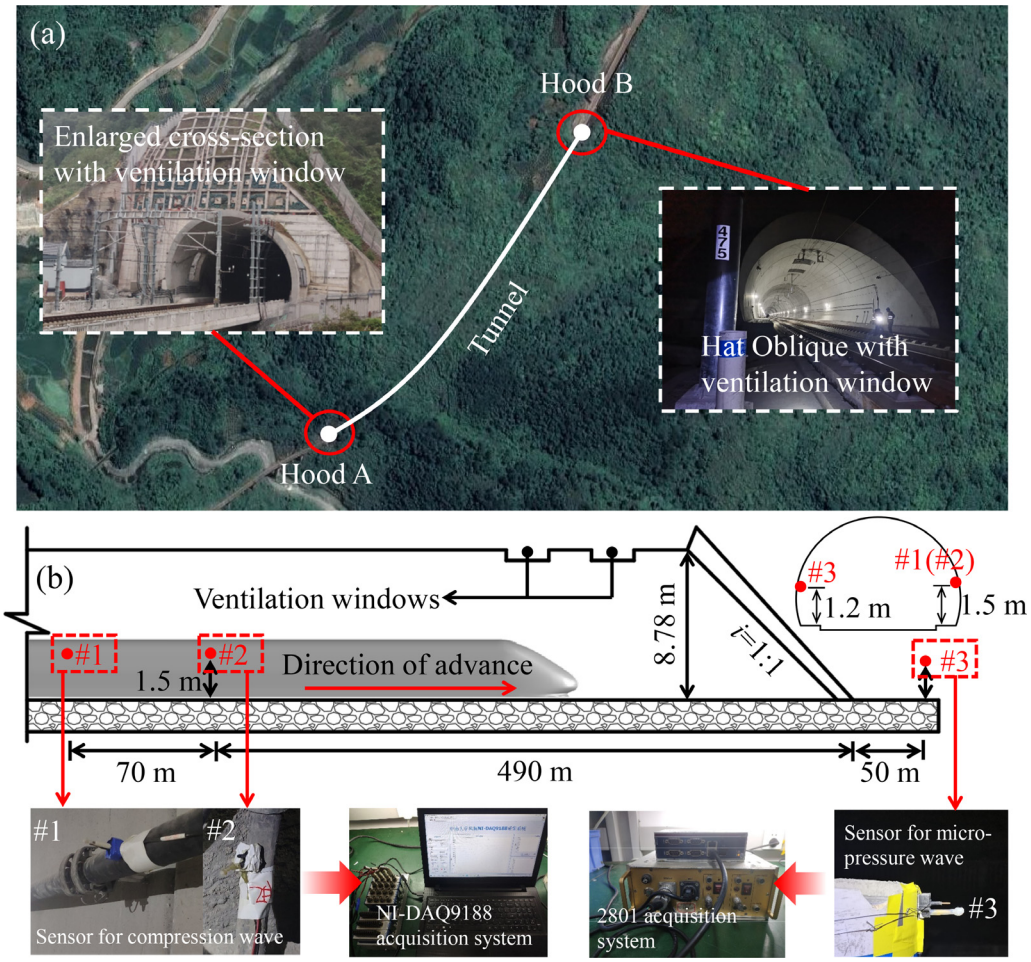

FIG. 2. Field measurement overview: (a) tunnel route and tunnel portal and (b) measurement scheme.

combination of a hat oblique buffer hood and ventilation windows, spanning a length of 31 m. The hat oblique Sec. of Hood B is 10.28 m long with a slope ratio of 1:1, and the top has two ventilation windows, each measuring 2×4 m^2. For the tests, the train traveled from hood A to hood B, and three separate tests were conducted, referred to as test 1, test 2, and test 3.

The DOC030NDC4 micro-pressure sensor produced by Honeywell is used during the measurements with an accuracy of 0.5%. The micro-pressure sensor in the tunnel has a range of ± 7500 Pa, and the micro-pressure sensor outside the tunnel has a range of ± 600 Pa. An A/D board and a 2801 data acquisition system were utilized to collect the pressure data inside the tunnel and the MPW data outside the tunnel, respectively. The test is conducted with a sampling frequency set to 1000 Hz.[30] To process the collected data, FFT filters were used, using a low-pass filter type with a cutoff frequency of 20 Hz. The arrangement of the measuring points is shown in Fig. 2(b). Points #1 and #2 represent pressure measurement points on the tunnel wall, situated at distances of 560 and 490 m from the tunnel exit, respectively. These points are positioned approximately 1.5 m above the ground. By contrast, point #3 serves as a measurement point for the MPW at the tunnel exit, located 50 m outside the tunnel exit and positioned approximately 1.2 m above the ground.

B. Results of field measurement

The measured results of the pressure inside the tunnel (#1 and #2) and the MPW outside the tunnel (#3) are presented in Fig. 3. The propagation characteristics of the pressure wave are illustrated in Fig. 3(a). The compression wave and expansion wave are represented by red solid line and blue dotted line, respectively. Dark gray and light gray represent the head and tail of the train. The waveforms of the four curves are generally similar, with slight differences in peak values and timing of peak occurrences, where the ICW has a positive peak defined as P_{ICW+} and a negative peak defined as P_{ICW-}.

It can be seen from the Mach diagram in Fig. 3(a) that the compression and expansion waves cause the pressure to rise and fall as they propagate to the measurement point, and the pressure also falls as the train passes through the measurement point. In Figs. 3(a-I) and (a-II), for measurement point #1, the timing of P_{ICW+} and P_{ICW-} is consistent across the three tests. In test 2, the P_{ICW+} is approximately 1.35% higher than in test 1, and in test 3, it is 0.6% higher than in test 1.

08 January 2025 07:45:32

Published under an exclusive license by AIP Publishing

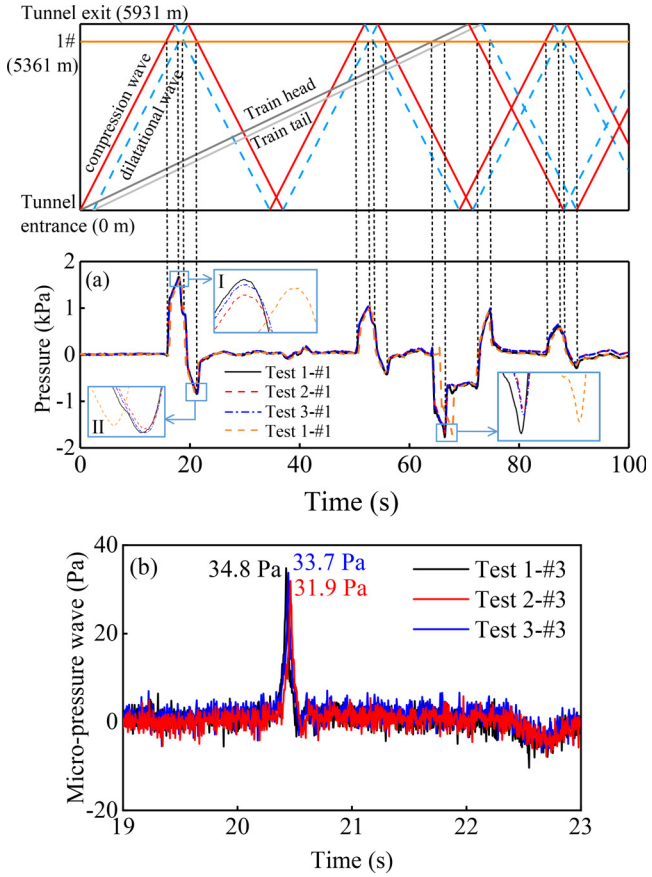

FIG. 3. Field measurement results: (a) measurement points #1 and #2 and (b) measurement point of #3.

The P_{ICW-} is approximately 0.85% higher in test 2, whereas it is nearly the same as test 3. In test 1, the P_{ICW+} between measurement points #1 and #2 have a difference of 0.74%. Additionally, a difference of 1.5% in the P_{ICW-} is found between the two measurement points. The occurrence of the P_{ICW+} is delayed by 0.25 s at measurement point #2 compared with measurement point #1, and the occurrence of the P_{ICW-} is delayed by 0.30 s. These differences deviate from the theoretical intervals of 0.21 s for the P_{ICW+} and 0.41 s for the P_{ICW-} by approximately 16% and 26.8%, respectively. As shown in Fig. 3(a-III), the negative peak values caused by the train passing at point #1 in the tunnel have almost the same occurrence time in all three tests. Compared with test 1, the negative peak values in test 2 and test 3 differ by 5.4% and 4.7%, respectively. In test 1, the negative peak values at #1 and #2 differ by 2.87%, and the occurrence time of the peaks differs by 1.1 s, which is 23.6% different from the theoretical time of 0.84 s required for the train to travel from measurement point #1 to measurement point #2. According to Fig. 3(b), the waveform and timing characteristics of the MPW at measurement point 3# are consistent across the three tests. The peak values appear at approximately the same time in all three tests. In test 1, the P_{MPW} at measurement point #3 is the highest, exceeding the P_{MPW} of test 2 and test 3 × 9.1% and 3.3%, respectively.

The errors mentioned above are influenced by factors such as train characteristics (variable speed, surface roughness), environmental conditions (temperature, humidity), and the sensitivity of the measuring instruments. Specifically, the air temperature and humidity vary during different time periods due to the time intervals in the field measurements of each group. As a result, the air density differs, impacting the propagation speed of the compression wave. For instance, test 1 is conducted in the morning, whereas test 2 is conducted at noon. In comparison to noon, the air temperature during the morning is lower, and the humidity is higher, resulting in a relatively greater air density. Consequently, the P_{ICW} and P_{MPW} observed during test 1 is larger. Given the difficulty in manually controlling these factors, the errors introduced by the testing method are considered acceptable.

III. METHODOLOGY

A. CFD model

A three-dimensional CFD dynamic grid simulation model of a tunnel–train–air system was established, as shown in Fig. 4(a), with the model representing the actual scale of the system. The tunnel in the simulation is a standard single-bore twin-track tunnel, 1000 m long, with a cross-sectional area of 100 m^2. In the train model's geometric parameters, the shape of the head train has the primary influence on the MPW. Therefore, a two-car formation with a length of 51.42 m, including the head train and the tail train, was selected.[10,31] Detailed structures such as bogies, pantographs, doors, and windows were not considered. The streamline head length (L_h) was set to 6.18 m, based on the design of the CRH380B model. The HEW's length is 60 m with a thickness of 0.5 m. The enlarged cross section has a cross-sectional area of 180 m^2 and is 40 m in length (L_2). The hat oblique section has a length (L_1) of 20 m, with a slope ratio of $i = 1{:}1.75$. The length of the ventilation windows is L_V, and the width is D_V. The atmospheric regions at both ends of the tunnel are modeled as rectangular cuboids. The dimensions of the cuboid at the entrance are 250 m (length), 200 m (width), and 100 m (height), whereas the dimensions of the cuboid at the exit are 210 m (length), 200 m (width), and 100 m (height). The sides, top, and back of the atmospheric region at the tunnel entrance are assigned the pressure–inlet boundary condition. For the atmospheric region at the exit of the tunnel, the sides, top, and back are assigned the pressure–far–field boundary condition.[32] Initially, the HST approaches the tunnel entrance from a distance of 150 m.

Figure 4(b) shows the arrangement scheme of monitoring points in the simulation. Monitoring point T1 is positioned at the top to observe the transient pressure variation pattern inside the tunnel, 100 m from the entrance. Monitoring points M1–M5 are positioned at 10 m intervals to observe the MPW variation pattern outside the tunnel. These points are located 1.5 m above the top of the rail.

B. Grid strategy and solution settings

Figure 5 shows the division of the computational domain using a combination of structured and unstructured grids based on the sliding grid technique.[33,34] To maintain a constant speed motion of 400 km/h for the HST, a velocity user-defined function is loaded. The overall grid region is divided into two parts: the static grid and the dynamic grid. Interfaces are used to facilitate information exchange between different regions during the flow field simulation.[35] The static grid is used for the buffer hood region, tunnel air, and the two end atmospheric

08 January 2025 07:45:32

Published under an exclusive license by AIP Publishing

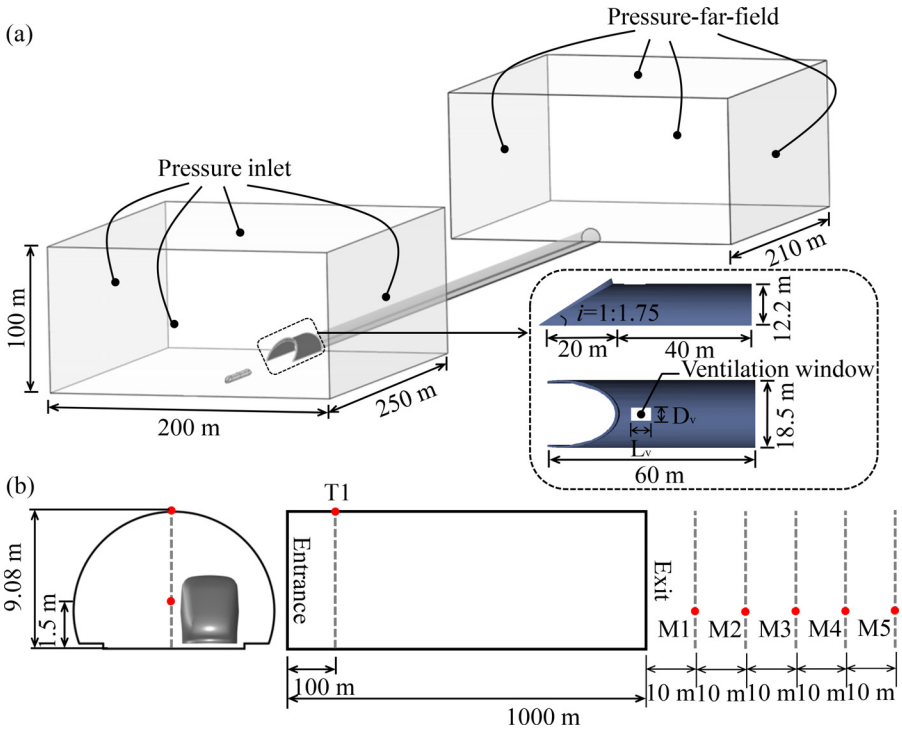

FIG. 4. Numerical calculation model: (a) geometric model and (b) monitoring point arrangement.

regions. The atmospheric region and tunnel air use structured grids composed of hexahedral elements. The buffer hood region is a rectangular core refinement region with dimensions of 90 m (length), 25 m (width), and 15 m (height), and it uses tetrahedral unstructured grids. The dynamic grid includes the areas near the train and the front and rear ballast regions. These areas also use structured grids composed of hexahedral elements. The grid size of the atmospheric region at both ends, the inside of the tunnel and the core encryption area, is controlled within 0.7, 0.5, and 0.1 m, respectively. The grid around the train is refined, with a maximum size of 1×10^{-3} m for the train surface grid. The train's surface is divided into 12 layers of attached surface layers, with an initial thickness of 4×10^{-5} m to achieve a y+ value[36] of approximately 10,[37] which is a parameter related to the near-wall treatment in CFD. The thickness of each layer in the boundary layer grid expands outward at a ratio of 1.2. The longitudinal grid size in the front and rear ballast regions is set to 1 m, providing sufficient resolution in these areas.

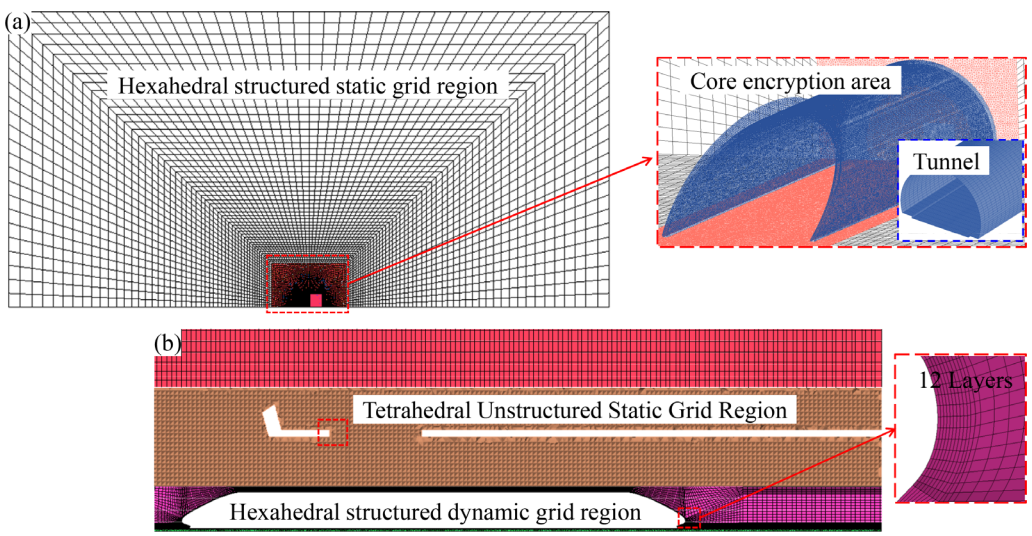

FIG. 5. Computational grid model.

08 January 2025 07:45:32

Published under an exclusive license by AIP Publishing

The IDDES[38,39] turbulence model based on SST k-ω was used in this study. The flow field has solved the pressure-based solver,[40,41] and the finite volume method was used to construct the discrete equations.[42] The second-order upwind scheme[43] was used for time integration and solving the momentum equations. The physical time step was set to 10^{-3}s with 50 iterations per step,[44,45] and[46] the minimum convergence criterion for residuals was 10^{-4}.

Grid resolution considerably influences computational accuracy and efficiency. Three different grid resolutions were established by adjusting the grid size in the core refinement region: coarse (10×10^6 cells), medium (20×10^6 cells), and fine (30×10^6 cells). The computational parameters of the models were kept consistent across the different grid resolutions.

Figure 6(a) provides diagrams of the three different grid schemes. The ICW at monitoring point T1 and the time history curve of the MPW at monitoring point M2 were compared as indicators. Figures 6(b) and 6(c) show that the pressure curves obtained from the fine and medium grids exhibit good consistency, whereas the pressure curve from the coarse grid shows considerable deviation. Comparing the P_{ICW} shows that the difference between the medium grid and coarse grid is 5.8%, whereas the difference with the fine grid is only 1.9%. Similarly, when comparing the P_{MPW}, the difference between the medium grid and the coarse grid is 7.1%, whereas the difference between the medium grid and the fine grid is only 3.2%. Based on the analysis of computational accuracy and efficiency, the model with a grid resolution of 20 million cells (medium grid) is considered a suitable compromise. This resolution provides a balance between computational accuracy and efficiency, yielding reliable results for further analysis and interpretation.

C. Model verification

As shown in Fig. 7(a), to further ensure the reliability of the tunnel–train–air dynamic grid aerodynamic simulation method described earlier, a 1:1 CFD model was established in this section, replicating the field measurement scenario. As depicted in Figs. 7(b) and 7(c), the numerical simulation results exhibit close resemblance to the observed trends in the ICW and MPW. Although slight differences are observed in the magnitude of fluctuations, the waveforms generally align. The field measurement process is subject to various irrelevant variables. For example, when compared to the numerical simulation, the measured tunnel and train nose are relatively rough, which increases the air resistance as the train passes through the tunnel. This roughness also leads to enhanced interaction between the compression wave and the tunnel wall. As a result, there is an increased possibility of wave reflection, causing significant fluctuations in the measured pressure curve compared to the simulated pressure curve. These factors generally introduce larger fluctuations in the measured pressure curves compared to the simulated ones. However, these differences do not considerably affect the overall consistency.

Specifically, the comparison reveals a 5.3% difference in the P_{ICW} at monitoring point #2 and a 5.5% difference in the P_{MPW} at monitoring point #3. While these discrepancies exist, they fall within an acceptable range of errors. Therefore, the numerical simulation method and its results are reliable. By conducting this comprehensive validation, the study strengthens the confidence in the accuracy and effectiveness of the numerical simulation approach. It provides valuable insights into the aerodynamic characteristics within the tunnel–train–air system and contributes to the further understanding and analysis of the phenomenon.

D. Research route

This study focuses on investigating the effect of two factors, namely, the ventilation window aperture ratio and the arrangement of ventilation windows (single, double, and triple), on the effectiveness of HEW in mitigating MPWs. The main objective of this study is to analyze the sensitivity of the ICW and its PG inside the tunnel, the MPW at the tunnel exit, and the flow field within the buffer hood to these two factors.

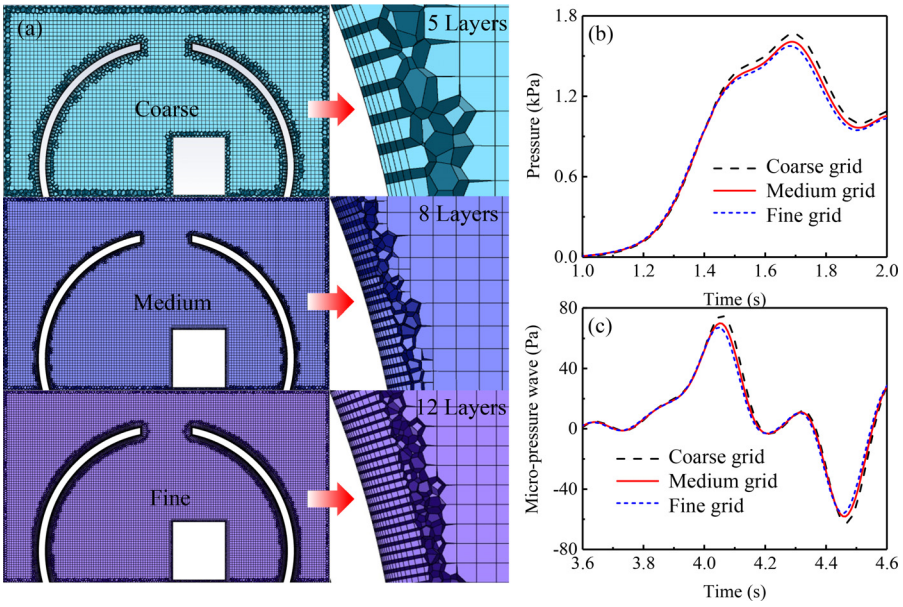

FIG. 6. Different grid schemes: (a) grids with different resolutions, (b) ICW in the monitoring points of T1, and (c) MPW in the monitoring point of M1.

08 January 2025 07:45:32

Published under an exclusive license by AIP Publishing

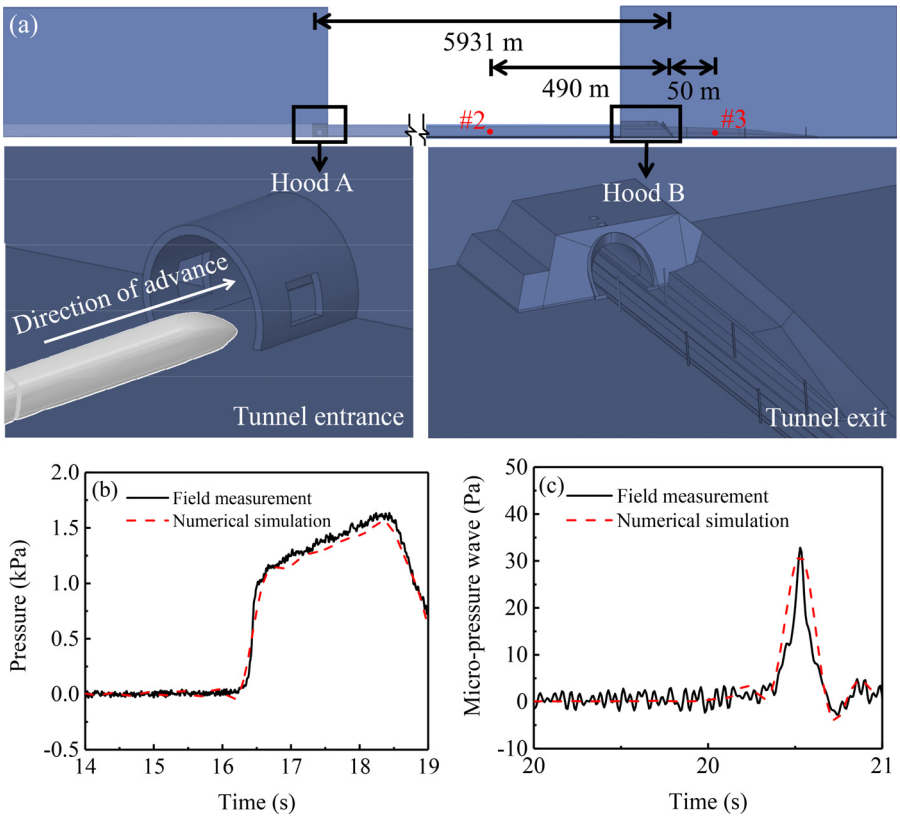

FIG. 7. Comparison of numerical simulation with field measurement: (a) numerical model, (b) ICW at monitoring point #2, and (c) MPW of monitoring point #3.

In Fig. 8, the proposed design conditions are presented. To avoid additional effects caused by changes in the position of the ventilation windows, the center of the ventilation window was fixed at the center of the top of the enlarged cross section, located 20 m away from the slope section end and tunnel entrance. The ventilation window's circumferential width (D_V) and longitudinal length (L_V) were adjusted by varying the central angle, defining the aperture ratio as $\alpha = D_V L_V / S_{\text{tunnel}}$. As a result, five different aperture ratio conditions were obtained: 0%, 8.95%, 15.92%, 24.87%, and 35.81%.

In the case of a single ventilation window, the MPW is associated with the streamline length of the streamline head (L_h).[47] Therefore, the distance from the center of the ventilation window to the slope section, end is defined as D, with different values of D being n(1, 2, 4, and 6) times L_h. The position coefficient (d) is defined as D/L_2 representing the relative position of the ventilation window in the enlarged cross section, where L_2 is the length of the enlarged cross section. Figure 8 illustrates six different arrangements for multiple ventilation windows. Cases 1–3 represent different layouts for double ventilation windows, while cases 4–6 depict various configurations for triple ventilation windows. The vertical distance between adjacent ventilation windows is either 7 or 14 m, and the distance between the lower edge of the circumferential ventilation window and the track surface is set at 3 m. These design conditions provide a comprehensive framework for investigating the impact of ventilation window aperture ratio and arrangement on mitigating MPW phenomena in combined buffer hoods.

IV. RESULTS AND DISCUSSION

A. Influence of the aperture ratio α

When an HST with a speed of 400 km/h passes through combined buffer hoods (HEW) with aperture ratios of 0% and 15.92%, the propagation characteristics of waves are depicted in Fig. 9. The black solid and red dashed lines denote the pressure and pressure gradient of the ICW, respectively, whereas the red solid and blue dashed lines denote the compression and expansion waves, respectively; the gray arrow represents the train's nose.

When the train's nose enters the hat structure end, the air inside the buffer hood is first compressed, generating a compression wave C_1 that propagates into the tunnel at the speed of sound. During the train's journey from the hat structure end to the slope section end, the spatial confinement increases, leading to a greater compression of the air. Subsequently, as the train's nose passes through the slope section end, a compression wave C_2 is generated and propagates into the tunnel. When C_2 reaches monitoring point T1, PG exhibits its first peak, labeled A1. In comparison with the case with an aperture ratio of 0% for the ventilation windows, A1 decreases by approximately 30% when the aperture ratio of the ventilation windows is 15.92%. Similarly, when the train enters the tunnel entrance, the cross-sectional area decreases from 180 to 100 m^2, resulting in an increased blockage ratio. As a result, the air inside the tunnel is compressed again, and a compression wave C_3 is emitted into the tunnel. C_3 is the reason for the second peak of PG, labeled A2. The study by Howe *et al.* Howe *et al.*[48] provides a theoretical explanation for the occurrence of

08 January 2025 07:45:32

Published under an exclusive license by AIP Publishing

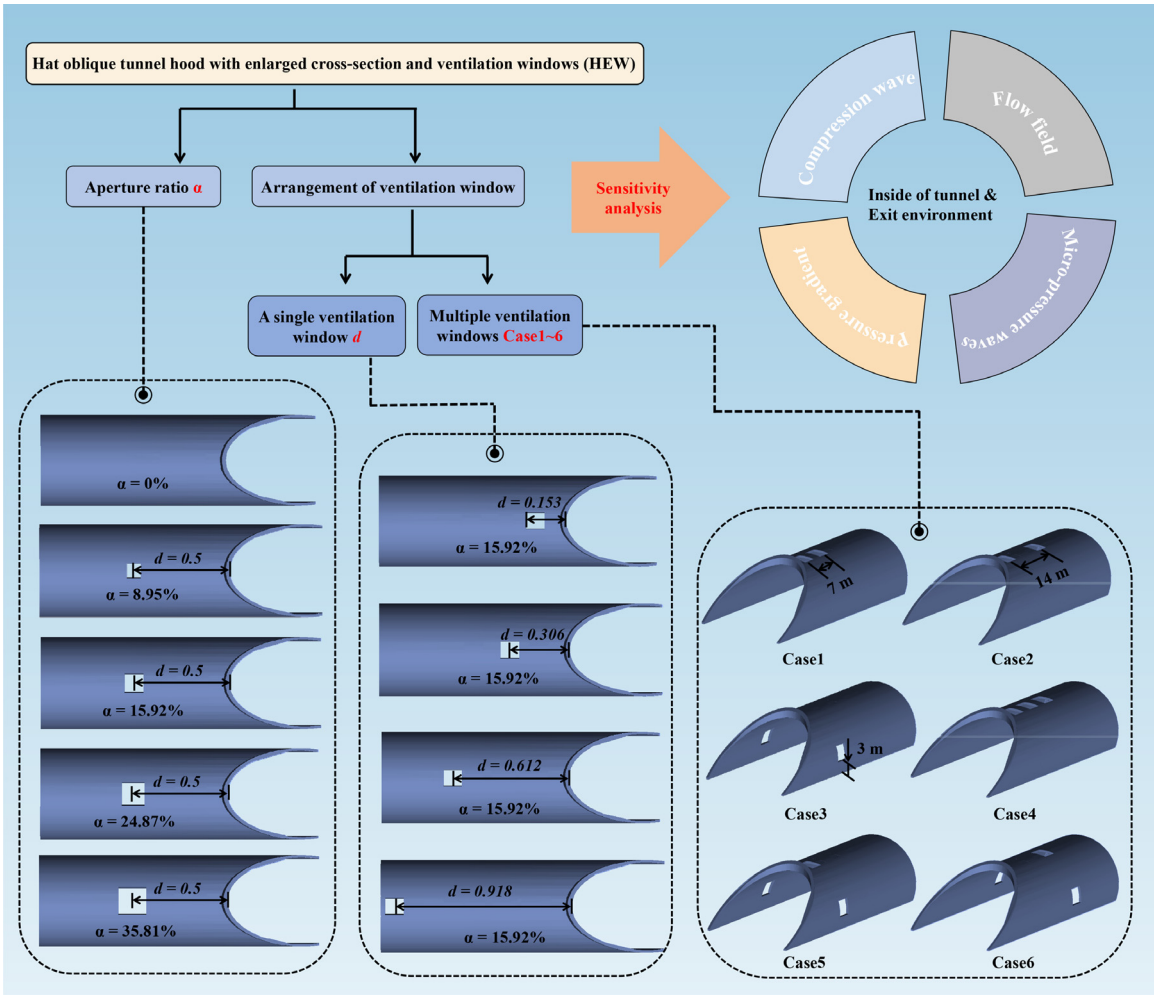

FIG. 8. Design condition.

the third peak of PG, labeled A3. It states that when the train enters the tunnel from the buffer hood, it emits an expansion wave E_3 toward the exit. E_3 propagates to the buffer hood entrance or the ventilation window, where it reflects into the tunnel in the form of a compression wave C_{3b}. This reflection of C_{3b} causes A3. In the case of a 0% aperture ratio, E_3 only reflects at the slope section cut, generating compression waves C_{3b1} and C_{3b2}. However, in the case of a 15.92% aperture ratio, an additional reflection occurs at the ventilation window, resulting in the generation of compression wave C_{3bv}. C_{3b1}, C_{3b2}, and C_{3bv} are collectively referred to as C_{3b}. Given the presence of the ventilation window, the reflection of E_3 occurs at an additional time, resulting in a 64.8% reduction in A3 in the case with the ventilation window. When the train passes through the ventilation windows, it compresses the air to a certain extent, and the degree of compression is related to the size of the windows. The compression wave C_V generated by the compressed air at the compression ventilation window causes the trough between A1 and A2 to become shallower. The rising time of the ICW will be advanced, and it will also have a "lift effect" on A2. These effects are disadvantageous for alleviating P_{MPW}.

To further compare the aerodynamic buffering effects of different combined buffer hoods (HEW) under various aperture ratios, Fig. 10 provides a comparison of the time-history curves at monitoring points T1 and M2. The figure also includes blue arrows indicating the time point at which the compression wave propagates to monitoring points T1 and M2. Figure 10(a) shows that under different aperture ratio conditions, the ICW and PG waveforms at T1 are essentially consistent, and their variation patterns are generally in agreement. As the aperture ratio increases, the P_{ICW} also increases, but it tends to stabilize gradually. Among them, the P_{ICW} differs by 14.8% between the aperture ratios of 0% and 35.81%, whereas the P_{ICW} between the aperture ratios of 24.87% and 35.81% differs by only 0.1%.

Compared with the ICW, the PG is more sensitive to changes in the aperture ratio. As the aperture ratio increases, A1 and A3 decrease gradually, whereas A2 increases gradually. When the aperture ratio is small, the compression wave C_V does not cause an earlier appearance of the trough between A1 and A2. For example, when $\alpha = 8.95\%$, the trough appears at the same time as when $\alpha = 0\%$. However, for aperture ratios greater than 8.95%, the trough tends to appear

08 January 2025 07:45:32

Published under an exclusive license by AIP Publishing

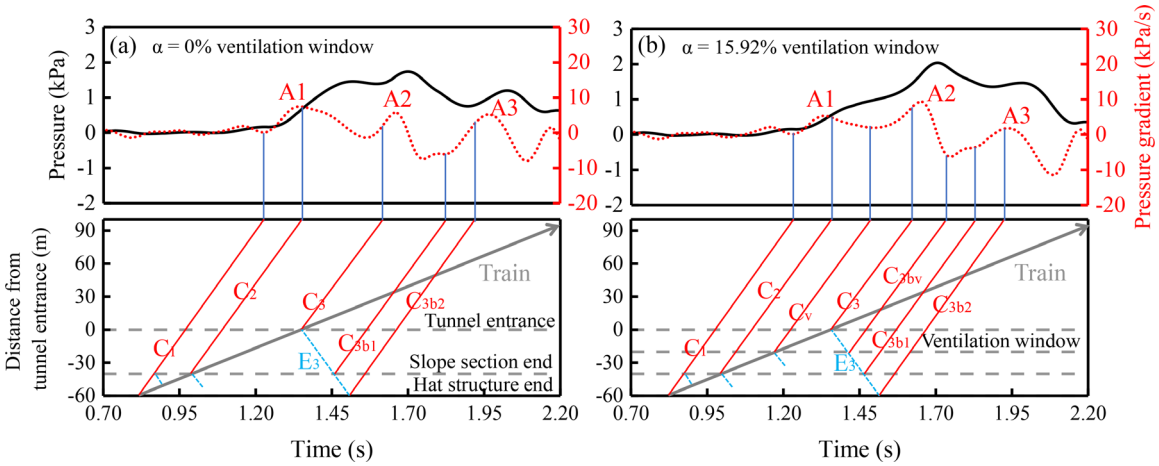

FIG. 9. Propagation characteristics of waves: (a) with an $\alpha = 0\%$ ventilation window and (b) with an $\alpha = 15.92\%$ ventilation window.

approximately 0.1 s earlier. Compared with the condition with a 0% aperture ratio, under the combined effect of the "advance effect" and "lift effect" of the C_V, the trough between A1 and A2 becomes shallower and A2 becomes larger. This coincides with the findings of Miyachi *et al.*[49,50] Compared with the conditions with 0% and 8.95% aperture ratios, A1 is reduced by 45.2% and 35.2%, respectively, for the 35.81% aperture ratio. By contrast, A2 is increased by 86.7% and 51.5%, respectively, whereas A3 is reduced by 76.8% and 50%. This results that A2 is more sensitive to changes in the aperture ratio.

Figure 10(b) shows the curves of the MPW at monitoring point M2 under different aperture ratio conditions. The graph reveals that the variation pattern of the MPW is generally consistent across different aperture ratios. However, differences are observed in terms of the P_{MPW} and the number of peaks in the MPW. The P_{MPW} in the graph, labeled P1 and P2, are observed. Additionally, using blue arrows, the times at which compression waves C_1, C_2, and C_3 propagate to M2 are marked. Moreover, compression waves C_1, C_2, and C_3 are the main causes of the formation of P1 and P2. As the aperture ratio increases, P1 gradually decreases, whereas P2 increases. Compared with the condition with a 0% aperture ratio, P1 decreases by 58.3%, and P2 increases by 542.5% for the condition with a 35.81% aperture ratio.

According to the MPW control specification,[29] the control of MPW requires attention to the maximum value between P1 and P2. The P_{MPW} at the 20 m position from the tunnel exit should not exceed 50 Pa. Based on the given values, when the aperture ratio α is 15.92%, the maximum value between P1 and P2 is 48 Pa, which meets the specification requirement of not exceeding 50 Pa at the 20 m position from the tunnel exit. However, for the other aperture ratios, the maximum values exceed the specified limit, indicating that the MPW does not meet the control requirements according to the given specification.

According to Fig. 11, for different aperture ratios (0%, 8.95%, 15.92%, 24.87%, and 35.81%) at distances of 10, 20, 30, 40, and 50 m from the tunnel exit, nonlinear surface fitting was performed using the Rational2D and Levenberg–Marquardt optimization algorithms. The surface equation is given by $z = (237.967\,42 + 0.041\,09x - 14.545\,69y + 0.339\,54y^2 - 0.002\,83y^3)/(1 + 0.052\,55x - 0.002\,45x^2 + 2.805\,91 \times 10^{-5}x^3 - 0.011\,25y - 7.872\,42 \times 10^{-5}y^2)$, where x, y, and z represent the aperture ratio α, the distance from the tunnel exit, and the P_{MPW}, respectively. The fitted equation shows a high correlation coefficient of $R^2 = 0.97$. This equation allows for the prediction of P_{MPW} at different aperture ratios and distances. Figure 11(b) represents the projection of the fitted surface onto the x–y plane, and the orange curve

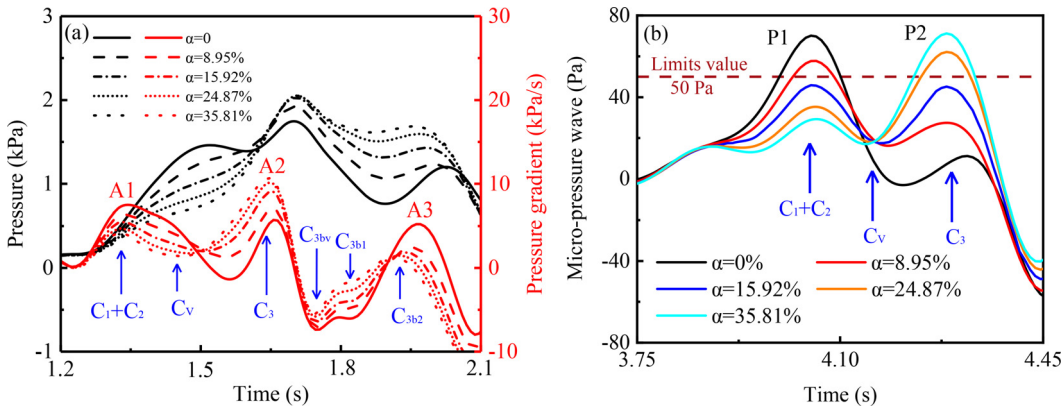

FIG. 10. Time history curves under different aperture ratios α: (a) ICW and PG of T1 and (b) MPW of M2.

08 January 2025 07:45:32

Published under an exclusive license by AIP Publishing

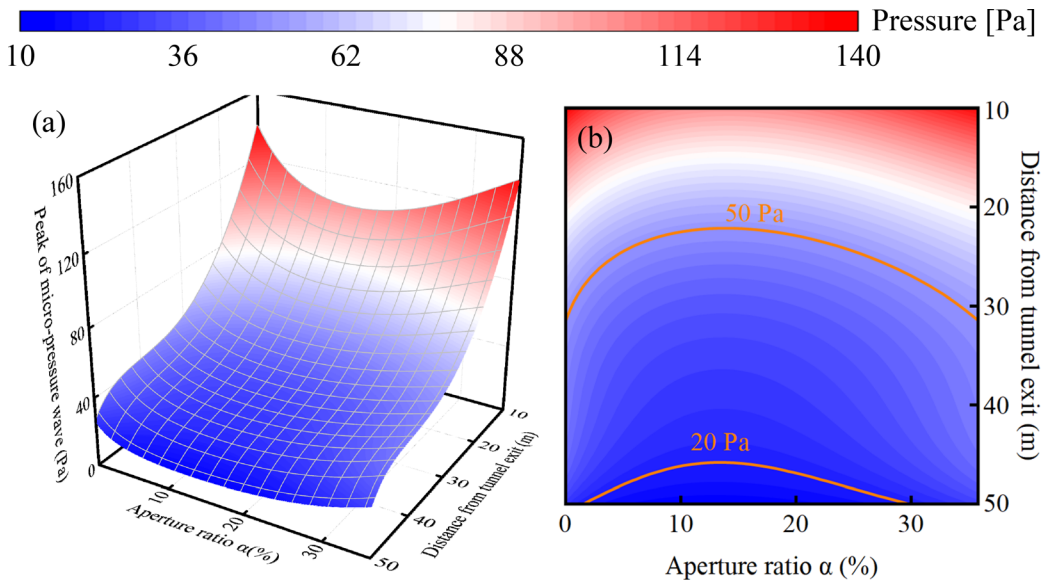

FIG. 11. P_{MPW} at M1–M5 with different aperture ratios: (a) peak fitting surface and (b) peak contour map.

indicates the specification limits at the tunnel entrance of 20 and 50 m (50, 20 Pa). The figure shows that for the same aperture ratio, as the distance from the exit increases, the P_{MPW} gradually decreases, and the rate of attenuation decreases. Under the same distance from the tunnel exit, the most effective aperture ratio for mitigating the P_{MPW} is approximately 15%. Optimizing the aperture ratio of a single ventilation window alone may not be sufficient to reduce the P_{MPW} within the 20 m range from the tunnel exit to below the specified limit of 50 Pa.

B. Influence of the arrangement of ventilation windows

1. Single ventilation window

Figure 12 depicts the propagation characteristics of waves when an HST with a speed of 400 km/h passes through combined buffer hoods with a constant aperture ratio of 15.92% at $d = 0.153$ and $d = 0.612$. Similar to the previous section, when the train passes through the hat structure end, slope section end, ventilation window, and tunnel entrance, compression waves C_1, C_2, C_V, and C_3 are generated and propagate into the tunnel. C_2 generates peak A1 in the PG, whereas C_3 generates peak A2 in the PG. The reflected wave C_{3b} from the expansion wave E_3 triggers peak A3 in the PG. The different positions of a single ventilation window result in variations in the time at which the compression wave C_V is generated. Compared with the condition with $d = 0.612$, when $d = 0.153$, the C_V is generated and propagates to monitoring point T1 approximately 0.17 s earlier, leading to the emergence of a new peak, denoted as A_V, following A1. By contrast, for the condition with $d = 0.612$, the appearance of A_V is relatively delayed. A2 increases, whereas the ICW rises at a faster rate, resulting in an increased peak magnitude.

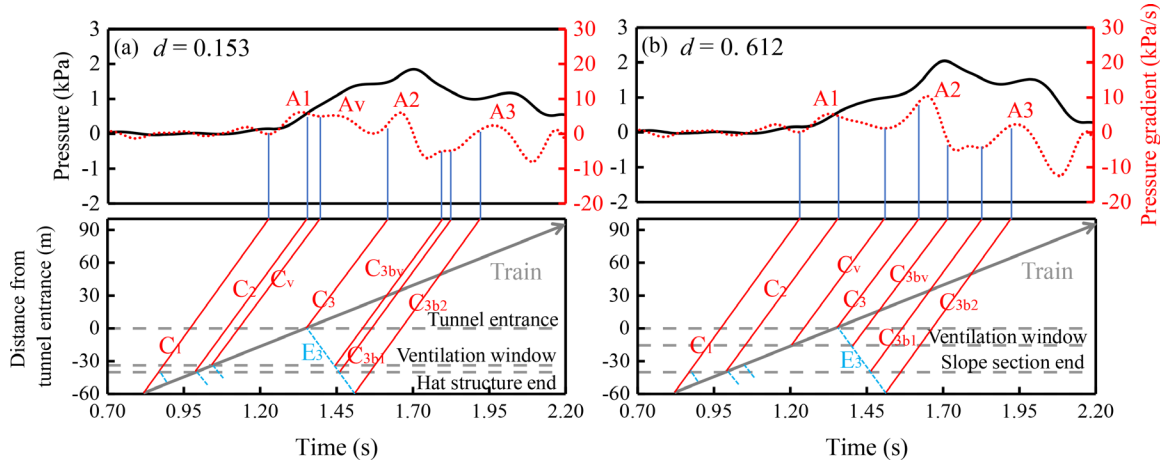

FIG. 12. Propagation characteristics of waves: (a) $d = 0.153$ and (b) $d = 0.612$.

08 January 2025 07:45:32

Published under an exclusive license by AIP Publishing

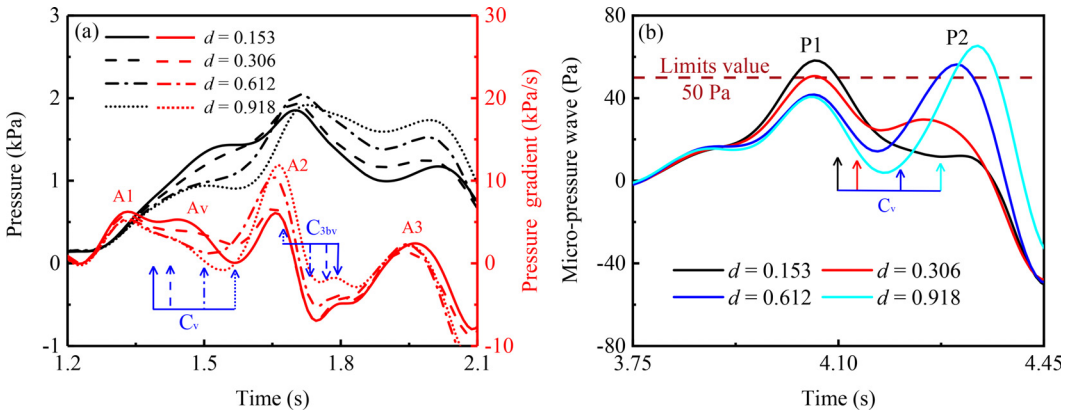

FIG. 13. Time history curves under different position coefficients *d*: (a) ICW and PG of T1 and (b) MPW of M2.

To compare further the effects of different positions of a single ventilation window on the buffering performance, Fig. 13 provides a comparison of the curves at monitoring points T1 and M2. The figure also includes blue arrows indicating the time point at which the compression wave propagates to monitoring points T1 and M2. As the position coefficient d increases, the time for C_V to propagate to monitoring point T1 becomes later, with a relative delay of $\Delta t_1 = (D_{i-1} - D_i)/V$. By contrast, the time for C_{3bv} to propagate is the opposite, with a relative advance of $\Delta t_2 = [2(D_{i-1} - D_i)]/c_0$, where D_i, V, and c_0 represent the distance from the center of the ventilation window to the slope section end, the speed of the train, and the speed of sound, respectively.

As shown in Fig. 13(a), compared with the $d = 0.153$ condition, the A1 for the $d = 0.306$, 0.612, and 0.918 conditions decreased by 6.8%, 14.4%, and 17.1%, respectively. A2 increased by 9.7%, 70.7%, and 95.2% for the respective conditions, indicating that A2 is more sensitive to the location of the ventilation window. As the position coefficient d increases, the time for A_V to appear becomes relatively delayed and gradually overlaps with A2, causing A2 to increase. This outcome leads to an accelerated rise rate and an increase in the P_{ICW}. When the ventilation window is closer to the tunnel entrance, C_{3bv} reflects into the tunnel earlier, resulting in a shallower trough between A2 and A3. As revealed in Fig. 13(b) analysis, when the ventilation window is positioned closer to the slope section end, the compression waves C_1, C_2, and C_V collectively contribute to P1. As the position coefficient d increases and the ventilation window moves backward, the contribution of C_V to P1 decreases, whereas its contribution to P2 increases. With increasing values of d relative to $d = 0.153$, P1 decreases by 13%, 28.2%, and 30.3% for the $d = 0.306$, 0.612, and 0.918 conditions, respectively. Meanwhile, P2 increases by 146.6%, 346.7%, and 444.5% for the respective conditions.

According to Fig. 14, for different position coefficients d (0.153, 0.306, 0.612, and 0.918) at distances of 10, 20, 30, 40, and 50 m from the tunnel exit, a nonlinear surface fitting was performed using the

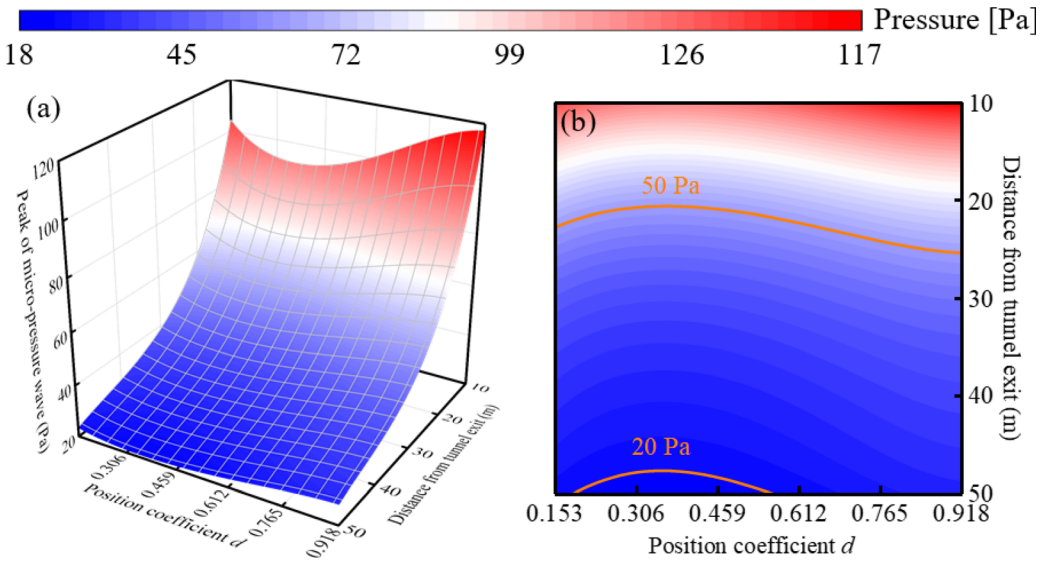

FIG. 14. P_{MPW} at M1–M5 with different position coefficients *d*: (a) peak fitting surface and (b) peak contour map.

08 January 2025 07:45:32

Published under an exclusive license by AIP Publishing

Rational2D and Levenberg–Marquardt optimization algorithms. The surface equation is given by $z = (423.187\,37 + 4.537\,74x - 18.382\,34y + 0.370\,21y^2 - 0.002\,96y^3)/(1 + 7.197\,54x - 13.519\,49x^2 + 6.885\,48x^3 + 0.098\,45y - 0.001\,67y^2)$, where x, y, and z represent the position coefficient d, distance from the tunnel exit, and P_{MPW}, respectively. The fitted equation shows a high correlation coefficient of $R^2 = 0.99$. Figure 14(a) presents the fitted surfaces of the P_{MPW} at measurement points M1–M5 for different position coefficients d. Figure 14(b) represents the projection of the fitted surface onto the x–y plane, and the orange curve indicates the specification limits at the tunnel entrance of 20 and 50 m (50, 20 Pa). Analysis of the figures reveals as the distance from the tunnel exit increases, P_{MPW} gradually decreases, and the rate of attenuation also decreases. With an increase in the position coefficient d, the efficiency of mitigating the P_{MPW} by a single ventilation window first increases and then decreases, with the most effective position coefficient ranging from approximately 0.3 to 0.4. However, optimizing the position coefficient of a single ventilation window alone is challenging to reduce the P_{MPW} below the specified limit of 50 Pa within a range of 20 m from the tunnel exit.

2. Multiple ventilation windows

Figure 15 shows the time–history curves of the IPW and PG for six different arrangements of multiple ventilation windows (double ventilation windows and triple ventilation windows). The blue arrows indicate the time at which some compression waves propagate to monitoring point T1.

As shown in Fig. 15(a), the rise time and peak appearance time of the ICW are generally consistent among the six configurations. However, differences are observed in the P_{ICW}. When there are two ventilation windows, the P_{ICW} of case 2 is the highest, followed by case 1, and case 3 has the lowest peak value. Additionally, when two ventilation windows are arranged in the longitudinal direction at the top of the HEW, the P_{ICW} is higher than when two ventilation windows are arranged in the circumferential direction. Compared with case 3, the P_{ICW} in case 1 remains almost unchanged, whereas in case 2, the peak has increased by 7.28%. When there are three ventilation windows, case 6 has the highest P_{ICW}, followed by case 4, and case 5 has the lowest peak. Compared with case 5, the P_{ICW} of cases 4 and 6 increased by 5.98% and 9.63%, respectively.

As shown in Fig. 15, when multiple ventilation windows are located near the slope section end, the A_V becomes more prominent. However, A3 is relatively smaller than to A1, Av, and A3; thus, it will not be further discussed. Analyzing Figs. 15(a)–15(f), it can be concluded that when there are two or three ventilation windows, Av is considerably higher when the ventilation windows are positioned in the radial direction of the HEW compared with that when they are positioned at the top. For example, the Av of case 3 is 46.6% higher than that of case 1, and the Av of case 5 is 67.2% higher than that of case 4. Comparing Figs. 15(a) and 15(b) reveals that when there are two ventilation windows, case 2 shows a decrease of 8.3% in A1 compared with case 1, whereas A2 increases by 18.6%. Similarly, comparing Figs. 15(e) and 15(f) reveal that when there are three ventilation windows, case 6 shows a decrease of 53% in A1 and an increase of 63% in A2 compared with case 5. The backward movement of the ventilation windows leads to a decrease in A1 and a delayed appearance of Av. Finally, Av coincides with A2, resulting in an increase in A2.

Figure 16(a) shows the time–history curves of the MPW at monitoring point M2 for cased 1–6. The red dashed line represents the specified limit (50 Pa) that the MPW needs to meet at a distance of 20 m from the tunnel exit. Similarly, the two peaks of the MPW are denoted as P1 and P2. As shown in the graph, multiple ventilation windows have a better alleviating effect on the MPW compared with a single ventilation window. The difference between P1 and P2 decreases, and the trough becomes shallower. Among them, only cases 4 and 6 fail to meet the specifications for the MPW, exceeding the limit by 15.4% and 71.1%, respectively. When there are two ventilation windows, all cases can reduce the MPW at the tunnel entrance to below the specified limit. Among them, case 1 exhibits the best mitigation effect on the MPW.

As shown in Fig. 16(b), for the MPW within the range of 10–50 m outside the tunnel exit, case 1 exhibits the best mitigation effect, whereas case 6 has the poorest mitigation effect. At the positions of 20 and 50 m outside the tunnel exit, P_{MPW} in case 1 is reduced by 101% and 108.6%, respectively, compared with case 6. Compared with the P_{MPW} at the tunnel exit of 20 m without any buffer hood (127 Pa) and with $\alpha = 0\%$ (70 Pa), case 1 reduces the peak values by 66.4% and 39.3%, respectively.

C. Discussion of the flow field mechanism

To reveal the mitigation mechanism of the ventilation windows further, Fig. 17 presents the horizontal pressure cloud diagram in longitudinal and transverse sections at three different time instances (t_1, t_2, and t_3). The figure illustrates three different aperture ratios α (0%, 15.92%, and 35.81%) and includes three contour lines representing different pressure levels, where t_1 represents the moment when the train's nose enters the HEW, t_2 represents the moment when the train's nose passes through the ventilation window, and t_3 represents the moment when the train's nose enters the tunnel.

As shown in Figs. 17(a_1)–17(c1), at time t_1, a considerable positive pressure region is found at the front end of the train's nose, whereas a negative pressure region appears in the transition area from the nose to the body of the train. As shown in Figs. 17(a_2)–17(c_2), from time t_1 to t_2, as some gas escapes outward through the ventilation windows, the pressure inside the HEW decreases. With an increase in the aperture ratio, PG peak A1 decreases. This result indicates that increasing the aperture ratio can mitigate the pressure waves C1 and C2 generated when the train enters the HEW. Specifically, with an increase in the aperture ratio, the MPW peak P1 gradually decreases because a higher aperture ratio allows for more gas to be released, resulting in a reduced pressure buildup and P_{MPW}. In Figs. 17(a_2)–17(c_2), at t_3, the corresponding peak pressures further increase. However, a minor difference is observed in the pressure in front of the train for different aperture ratios because the P_{ICW} is primarily determined by the blockage ratio and the train speed.[51] The aperture ratio of the ventilation windows mainly affects the PG rather than considerably altering the magnitude of the ICW. Therefore, during the process from t_2 to t_3, with an increase in the aperture ratio, PG peak A2 also increases, intensifying the compression wave C_3 and resulting in an increase in the MPW second peak P2.

Figure 18 shows the horizontal pressure cloud diagram of the longitudinal section at three different time instances (t_1, t_2, and t_3) for cases 1–6. In Figs. 18(a)–18(c), at time t_1, the pressure inside the HEW with radially arranged ventilation windows is slightly lower than the

08 January 2025 07:45:32

Published under an exclusive license by AIP Publishing

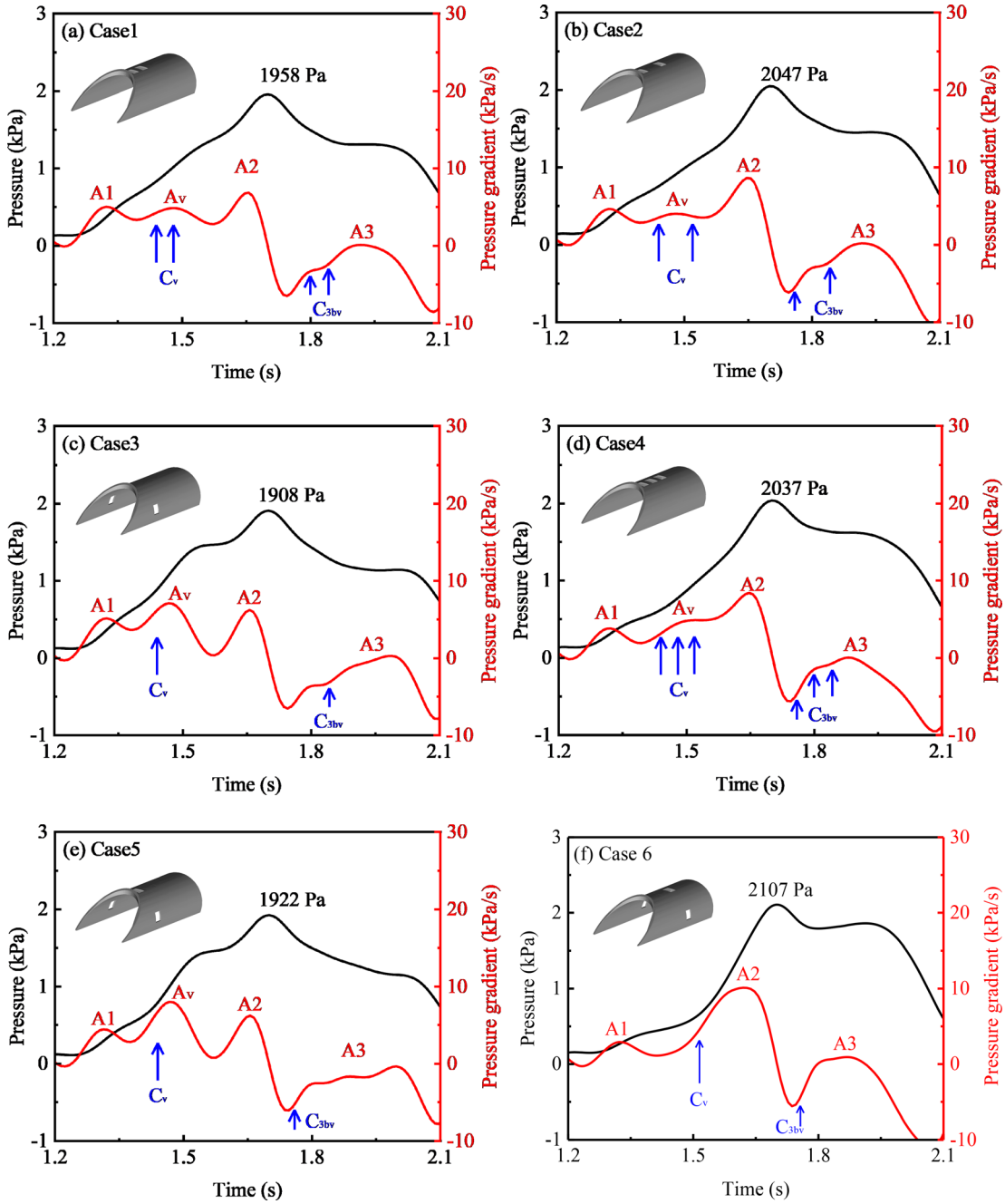

FIG. 15. ICW and PG of T1 with multiple ventilation windows: (a)–(f) represent cases 1–6, respectively.

pressure inside the HEW with ventilation windows arranged at the top. This result occurs because the two radially arranged ventilation windows are closer to the train, resulting in a greater amount of high-pressure gas escaping in the same timeframe. However, when the ventilation windows are arranged at the top, the time for high-pressure air to escape from the ventilation windows is prolonged, resulting in a noticeable difference in pressure inside the HEW at time t_2. Among them, case 3 leads to more pronounced pressure changes in the compression waves C_1 and C_2 during the t_1 to t_2 process, with a higher peak A1 in the PG. Comparing Figs. 18(e) and 18(f) at moments t_1 and t_2 reveals that as the ventilation windows move toward the tunnel entrance, the time for high-pressure gas to escape from the ventilation windows is prolonged, resulting in a decrease in peak A1 in the PG. Therefore, placing the ventilation windows near the tunnel entrance

08 January 2025 07:45:32

Published under an exclusive license by AIP Publishing

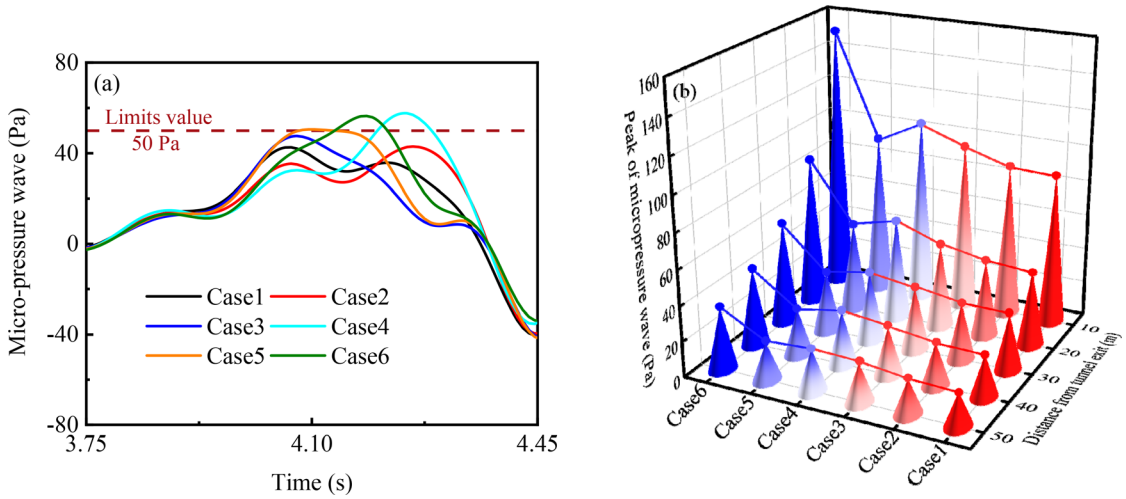

FIG. 16. MPW of cases 1–6: (a) time history curve of MPW of M2 and (b) P_{MPW} of M1–M5.

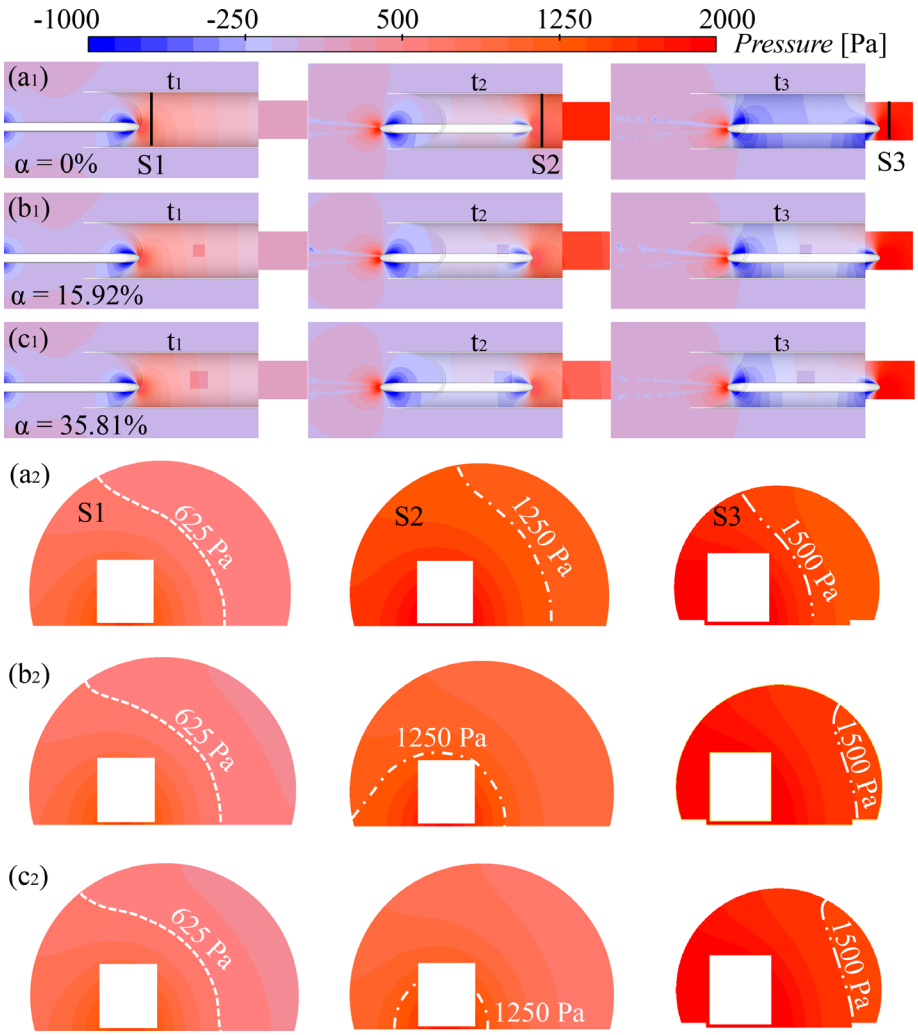

FIG. 17. Horizontal pressure cloud diagram with different aperture ratios: (a_1)–(c_1) longitudinal section and (a_2)–(c_2) transverse section.

08 January 2025 07:45:32

Published under an exclusive license by AIP Publishing

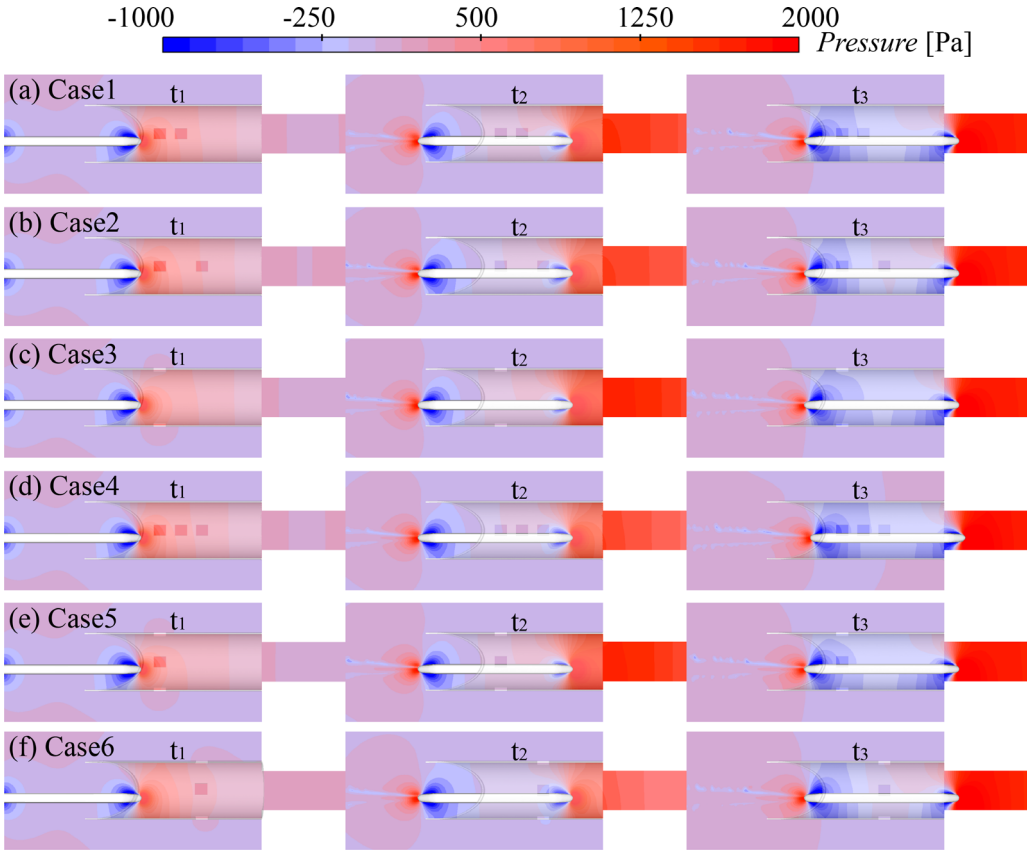

FIG. 18. Horizontal pressure cloud diagram of the longitudinal section with cases 1–6.

can alleviate compression waves C_1 and C_2, ultimately leading to a reduction in the MPW first peak P1. At t_3, the placement of ventilation windows near the tunnel entrance has a minimal effect on the pressure waves generated when the train enters the tunnel. Comparing t_2 and t_3 reveals that during the process of the train passing through the ventilation windows and entering the tunnel, the closer the ventilation windows are to the tunnel entrance, the more remarkable the pressure changes are. As a result, the compression wave C_3 leads to a higher PG peak A2 in the ICW. Placing the ventilation windows closer to the tunnel entrance enhances the C_3 generated when the train enters the tunnel, leading to a gradual increase in the second peak P2 of the MPW.

The effect of prolonging the venting time is more pronounced in the escape of high-pressure air. Comparing the t_2 moment in Figs. 18(c)–18(e) reveals that increasing the number of ventilation windows at the top of the HEW, although increasing the amount of high-pressure air escaping within the same time frame, results in considerably lower pressure inside the HEW of case 4 compared to case 5. By contrast, the pressure inside the HEW of case 5 shows relatively unremarkable changes compared with case 3. Comparing Figs. 18(a) and 18(d) reveals that adding ventilation windows at the top of the HEW prolongs the escape time of high-pressure air, resulting in a decrease in the first peak P1 of the MPW. However, this also increases the PG peak A2 of the ICW, which is unfavorable for the mitigation of the second peak P2 of the MPW in the HEW.

V. CONCLUSION

This study systematically investigates and discusses the mitigation mechanism and sensitivity of ventilation window parameters in the HEW for a 400 km/h high-speed railway tunnel. The research begins with field measurements conducted in an actual railway tunnel. Subsequently, a series of CFD simulations was performed using the IDDES turbulence model and sliding grid technique. The reliability of the simulation approach is validated against field measurements. The main conclusions drawn from this study are as follows:

(1) The field measurements, conducted three times, showed a difference within 2% for positive and negative P_{ICW} and a maximum difference of 8.11% for P_{MPW}. Comparison of these field measurements with the numerical simulations showed a difference of 5.3% for positive P_{ICW} and 5.5% for P_{MPW}. These results confirm the reliability of the numerical simulation method and its results.
(2) With the increase of the aperture ratio of the ventilation window, the compression wave generated by the train entering the tunnel from HEW is weakened, but the compression wave generated by the train entering the tunnel from HEW is intensified. Consequently, P_{MPW} initially decreases and then increases. The fitting results of the aperture ratio and P_{MPW} show that the optimal aperture ratio is about 15% when a single ventilation window is used.

08 January 2025 07:45:32

Published under an exclusive license by AIP Publishing

(3) When the ventilation window is located closer to the tunnel entrance, the duration of high-pressure air outflow is increased. This reduces the generation of compression waves as the train enters the HEW. However, it intensifies the compression waves generated when the train enters the tunnel from the HEW. Consequently, the P_{MPW} initially decreases and then increases. When the distance between the ventilation window and the end of the slope section is about 0.3–0.4 times the enlarged section of the HEW, the mitigation effect on MPW is the best.
(4) Compared to single- and triple-ventilation window configurations, using a double-ventilation window configuration is the most effective in reducing MPW. Placing the ventilation windows longitudinally at the top of the HEW promotes the outflow of high-pressure air more effectively than placing them circumferentially. However, excessive overflow hinders control over the second peak of the MPW.

The arrangement of multiple ventilation windows was based on equal aperture ratios in this study, which has certain limitations in achieving the optimal buffering effect of the HEW. In the future, the focus will be on studying the arrangement of ventilation windows with nonuniform aperture ratios. Additionally, factors such as different train speeds and tunnel lengths should be considered to address the adaptability of the HEW. This plan will help provide more comprehensive conclusions and further enhance the engineering value of the research.

ACKNOWLEDGMENTS

This work was funded by the National Natural Science Foundation of China (Grant No. 51978670), the Research Grants Council, University Grants Committee of the Hong Kong Special Administrative Region (SAR), China (Grant No. R-5020-18), the Innovation and Technology Commission of the Hong Kong SAR Government (Grant No. K-BBY1), the Hong Kong Polytechnic University's Postdoc Matching Fund Scheme (Grant No. 1-W21Q), and the Science and Technology Research and Development Program Project of China railway group limited (Major Special Project, 2021-Special-01).

AUTHOR DECLARATIONS

Conflict of Interest

The authors have no conflicts to disclose.

Author Contributions

Guo-Zhi Li: Software (lead), Writing – original draft (lead). **Xin Ye:** Software (equal), Validation (equal), Writing – review & editing (equal). **E Deng:** Methodology (lead), Data curation (lead), Writing – review & editing (lead), Funding acquisition (equal), Supervision (lead). **Wei-Chao Yang:** Conceptualization (lead), Funding acquisition (lead), Writing – review & editing (equal). **Yi-Qing Ni:** Writing – review & editing (equal), Funding acquisition (equal). **Hong He:** Software (equal). **Wai-Kei Ao:** Validation (lead).

DATA AVAILABILITY

The data that support the findings of this study are available from the corresponding author upon reasonable request.

REFERENCES

[1]Y. K. Liu, W. C. Yang, E. Deng, Z. W. Chen, and Y. Q. Ning, "Pressure amplification effect of initial compression waves in circumferential cracks of high-speed railway tunnel linings," Phys. Fluids **35**, 066119 (2023).
[2]J. Q. Niu, Y. Sui, Q. J. Yu, X. L. Cao, and Y. P. Yuan, "Aerodynamics of railway train/tunnel system: A review of recent research," Energy Built. Environ. **1**(4), 351–375 (2020).
[3]Y. K. Liu, E. Deng, W. C. Yang, Y. Q. Ning, Z. Zhou, and J. J. Zhang, "Aerodynamic intensification effect and dynamic response of cracks on high-speed railway tunnel linings," Tunnelling Underground Space Technol. **140**, 105308 (2023).
[4]S. Han, J. Zhang, X. H. Xiong, P. Ji, L. Zhang, J. Sheridan, and G. J. Gao, "Influence of high-speed maglev train speed on tunnel aerodynamic effects," Build. Environ. **223**, 109460 (2022).
[5]G. Zhang, T. H. Kim, D. H. Kim, and H. D. Kim, "Prediction of micro-pressure waves generated at the exit of a model train tunnel," J. Wind Eng. Ind. Aerodyn. **183**, 127–139 (2018).
[6]D. Uystepruyst, M. William-Louis, and F. Monnoyer, "3D numerical design of tunnel hood," Tunnelling Underground Space Technol. **38**, 517–525 (2013).
[7]X. T. Xiang, L. P. XUE, and B. L. Wang, "Aerodynamic effects of unvented hoods on the initial compression wave generated by a high-speed train entering a tunnel," ASME. J. Fluids Eng. **138**, 031102 (2016).
[8]T. H. Liu, H. Q. Tian, and X. F. Liang, "Design and optimization of tunnel hoods," Tunnelling Underground Space Technol. **25**, 212–219 (2010).
[9]X. T. Xiang, L. P. Xue, and B. L. Wang, "Aerodynamic effects of inclined portals on the initial compression wave generated by a high-speed train entering a tunnel," ASME. J. Fluids Eng. **137**, 121104 (2015).
[10]L. Zhang, H. Liu, N. Stoll, and K. Thurow, "Influence of tunnel aerodynamic effects by slope of equal-transect ring oblique tunnel portal," J. Wind Eng. Ind. Aerodyn. **169**, 106–116 (2017).
[11]Z. J. Guo, T. H. Liu, W. H. Li, and Y. T. Xia, "Parameter study and optimization design of a hat oblique tunnel portal," Proc. Inst. Mech. Eng., Part F **236**, 234–246 (2021).
[12]S. Saito and T. Fukuda, "Design of a tunnel entrance hood for high-speed trains," J. Wind Eng. Ind. Aerodyn. **206**, 104375 (2020).
[13]M. S. Howe, "Prolongation of the rise time of the compression wave generated by a high-speed train entering a tunnel," Proc. R. Soc. London, Ser. A **455**, 863–878 (1999).
[14]X. T. Xiang and L. P. Xue, "Tunnel hood effects on high speed train-tunnel compression wave," J. Hydrodyn. **22**, 897–947 (2010).
[15]S. Saito, "Optimizing cross-sectional area of tunnel entrance hood for high speed rail," J. Wind Eng. Ind. Aerodyn. **184**, 296–304 (2019).
[16]T. Fukuda and S. Saito, "Model experiments on the influence of tunnel hood cross sectional area on the reduction of the pressure gradient of the compression wavefront in high-speed railways," Mech. Eng. J. **10**(1), 22–00155 (2023).
[17]D. H. Kim, S. Y. Cheol, R. S. Iyer, and H. D. Kim, "A newly designed entrance hood to reduce the micro pressure wave emitted from the exit of high-speed railway tunnel," Tunnelling Underground Space Technol. **108**, 103728 (2021).
[18]L. Zhang, K. Thurow, N. Stoll, and H. Liu, "Influence of the geometry of equal-transect oblique tunnel portal on compression wave and micro-pressure wave generated by high-speed trains entering tunnels," J. Wind Eng. Ind. Aerodyn. **178**, 1–17 (2018).
[19]L. Zhang, M. Z. Yang, X. F. Liang, and J. Zhang, "Oblique tunnel portal effects on train and tunnel aerodynamics based on moving model tests," J. Wind Eng. Ind. Aerodyn. **167**, 128–139 (2017).
[20]F. Liu, S. Yao, J. Zhang, and Y. Q. Wang, "Field measurements of aerodynamic pressures in high-speed railway tunnels," Tunnelling Underground Space Technol. **72**, 97–106 (2018).
[21]F. Liu, J. Q. Niu, J. Zhang, and G. X. Li, "Full-scale measurement of micropressure waves in high-speed railway tunnels," ASME. J. Fluids Eng. **141**, 034501 (2019).
[22]M. S. Howe, "On the design of a tunnel-entrance hood with multiple windows," J. Sound Vib. **273**(1–2), 233–248 (2004).
[23]M. S. Howe, "On the role of separation in compression wave generation by a train entering a tunnel hood with a window," IMA J. Appl. Math. **70**(3), 400–418 (2005).

08 January 2025 07:45:32

Published under an exclusive license by AIP Publishing

[24]M. S. Howe, "The genetically optimized tunnel-entrance hood," J. Fluids Struct. **23**(8), 1231–1250 (2007).
[25]X. T. Xiang, L. P. Xue, B. L. Wang, and W. Zou, "Mechanism and capability of ventilation openings for alleviating micro-pressure waves emitted from high-speed railway tunnels," Build. Environ. **132**, 245–254 (2018).
[26]D. Heine, K. Ehrenfried, G. Heine, and S. Huntgeburth, "Experimental and theoretical study of the pressure wave generation in railway tunnels with vented tunnel portals," J. Wind Eng. Ind. Aerodyn. **176**, 290–300 (2018).
[27]T. Miyachi and T. Fukuda, "Model experiments on area optimization of multiple openings of tunnel hoods to reduce micro-pressure waves," Tunnelling Underground Space Technol. **115**, 103996 (2021).
[28]H. Okubo, T. Miyachi, and T. Fukuda, "Field test for micro-pressure wave reduction measurement by area optimization of windows of tunnel hoods," Proc. Inst. Mech. Eng., Part F **236**, 1262–1270 (2022).
[29]China State Railway Group Co. Ltd, *Code for Design of High Speed Railway–Part 8: Tunnel* (China State Railway Group Co. Ltd, 2014).
[30]China Railway Publishing House, *Technical Regulations for Dynamic Acceptance for High-Speed Railways Construction* (China Railway Publishing House, 2013).
[31]X. F. Liang, G. Chen, X. B. Li, and D. Zhou, "Numerical simulation of pressure transients caused by high-speed train passage through a railway station," Build. Environ. **184**, 107228 (2020).
[32]T. T. Wang, C. Hu, L. Zhang, X. D. Tian, F. C. Shi, and J. Y. Wang, "Research on the mechanism of micro-pressure waves in a high-speed train passing through a high geo-temperature tunnel," J. Wind Eng. Ind. Aerodyn. **226**, 105031 (2022).
[33]J. Q. Niu, Y. C. Zhang, R. Li, Z. W. Chen, H. D. Yao, and Y. M. Wang, "Aerodynamic simulation of effects of one- and two-side windbreak walls on a moving train running on a double track railway line subjected to strong cross-wind," J. Wind Eng. Ind. Aerodyn. **221**, 104912 (2022).
[34]D. H. Ouyang, W. C. Yang, E. Deng, Y. W. Wang, X. H. He, and L. B. Tang, "Comparison of aerodynamic performance of moving train model at bridge–-tunnel section in wind tunnel with or without tunnel portal," Tunnelling Underground Space Technol. **135**, 105030 (2023).
[35]W. H. Li, T. H. Liu, X. S. Huo, Z. W. Chen, Z. J. Guo, and L. Li, "Influence of the enlarged portal length on pressure waves in railway tunnels with cross-section expansion," J. Wind Eng. Ind. Aerodyn. **190**, 10–22 (2019).
[36]D. Lakehal, D. Métrailler, and S. Reboux, "Turbulent water flow in a channel at Re = 400 laden with 0.25 mm diameter air-bubbles clustered near the wall," Phys. Fluids **29**, 065101 (2017).
[37]Z. J. Guo, T. H. Liu, Z. Liu, X. D. Chen, and W. H. Li, "An IDDES study on a train suffering a crosswind with angles of attack on a bridge," J. Wind Eng. Ind. Aerodyn. **217**, 104735 (2021).
[38]X. S. Huo, T. H. Liu, Z. W. Chen, W. H. Li, H. R. Gao, and S. M. Wang, "Comparative analysis of the aerodynamic characteristics on double-unit trains formed by different types of high-speed train," J. Wind Eng. Ind. Aerodyn. **217**, 104757 (2021).
[39]K. He, X. C. Su, G. J. Gao, and S. Krajnović, "Evaluation of LES, IDDES and URANS for prediction of flow around a streamlined high-speed train," J. Wind Eng. Ind. Aerodyn. **223**, 104952 (2022).
[40]T. T. Wang, F. Wu, M. Z. Yang, P. Ji, and B. S. Qian, "Reduction of pressure transients of high-speed train passing through a tunnel by cross-section increase," J. Wind Eng. Ind. Aerodyn. **183**, 235–242 (2018).
[41]Z. W. Chen, Z. H. Guo, Y. Q. Ning, T. H. Liu, and J. Zhang, "A suction method to mitigate pressure waves induced by high-speed maglev trains passing through tunnels," Sustainable Cities Soc. **96**, 104682 (2023).
[42]H. Fang, X. X. Wu, X. Y. Zou, and X. F. Yang, "An integrated simulation-assessment study for optimizing wind barrier design," Agric. Meteorol. **263**, 198–206 (2018).
[43]W. C. Yang, H. Yue, E. Deng, Y. W. Wang, X. H. He, and Y. F. Zou, "Influence of the turbulence conditions of crosswind on the aerodynamic responses of the train when running at tunnel-bridge-tunnel," J. Wind Eng. Ind. Aerodyn. **229**, 105138 (2022).
[44]J. Muñoz-Paniagua, J. García, and A. Crespo, "Genetically aerodynamic optimization of the nose shape of a high-speed train entering a tunnel," J. Wind Eng. Ind. Aerodyn. **130**, 48–61 (2014).
[45]T. T. Wang, Y. Zhu, X. D. Tian, F. C. Shi, L. Zhang, and Y. B. Lu, "Design method of the variable cross-section tunnel focused on improving passenger pressure comfort of trains intersecting in the tunnel," Build. Environ. **221**, 109336 (2022).
[46]J. Q. Niu, D. Zhou, X. F. Liang, T. H. Liu, and S. Liu, "Numerical study on the aerodynamic pressure of a metro train running between two adjacent platforms," Tunnelling Underground Space Technol. **65**, 187–199 (2017).
[47]T. Miyachi, K. Kikuchi, and M. Hieke, "Multistep train nose for reducing micro-pressure waves," J. Sound Vib. **520**, 116665 (2022).
[48]M. S. Howe, M. Iida, and T. Fukuda, "Influence of an unvented tunnel entrance hood on the compression wave generated by a high-speed train," J. Fluids Struct. **17**, 833–853 (2003).
[49]T. Miyachi, S. Saito, T. Fukuda, Y. Sakuma, S. Ozawa, T. Arai, S. Sakaue, and S. Nakamura, "Propagation characteristics of tunnel compression waves with multiple peaks in the waveform of the pressure gradient: Part 1: Field measurements and mathematical model," Proc. Inst. Mech. Eng., Part F **230**, 1297–1308 (2016).
[50]T. Miyachi, S. Ozawa, M. Iida, T. Fukuda, and T. Arai, "Propagation characteristics of tunnel compression waves with multiple peaks in the waveform of the pressure gradient: Part 2: Theoretical and numerical analyses," Proc. Inst. Mech. Eng., Part F **230**, 1309–1317 (2016).
[51]R. S. Iyer, D. H. Kim, and H. D. Kim, "Propagation characteristics of compression wave in a high-speed railway tunnel," Phys. Fluids **33**, 086104 (2021).

08 January 2025 07:45:32

Published under an exclusive license by AIP Publishing